

A round Earth for climate models

Michael J. Prather^{a,1,2} and Juno C. Hsu^{a,1}

^aDepartment of Earth System Science, University of California, Irvine, CA 92697-3100

Edited by Dennis L. Hartmann, University of Washington, Seattle, WA, and approved August 8, 2019 (received for review May 16, 2019)

Sunlight drives the Earth's weather, climate, chemistry, and biosphere. Recent efforts to improve solar heating codes in climate models focused on more accurate treatment of the absorption spectrum or fractional clouds. A mostly forgotten assumption in climate models is that of a flat Earth atmosphere. Spherical atmospheres intercept $2.5 \text{ W}\cdot\text{m}^{-2}$ more sunlight and heat the climate by an additional $1.5 \text{ W}\cdot\text{m}^{-2}$ globally. Such a systematic shift, being comparable to the radiative forcing change from pre-industrial to present, is likely to produce a discernible climate shift that would alter a model's skill in simulating current climate. Regional heating errors, particularly at high latitudes, are several times larger. Unlike flat atmospheres, constituents in a spherical atmosphere, such as clouds and aerosols, alter the total amount of energy received by the Earth. To calculate the net cooling of aerosols in a spherical framework, one must count the increases in both incident and reflected sunlight, thus reducing the aerosol effect by 10 to 14% relative to using just the increase in reflected. Simple fixes to the current flat Earth climate models can correct much of this oversight, although some inconsistencies will remain.

solar radiation | spherical atmospheres | climate modeling

Our image of the atmosphere from space is that of a thin layer wrapped around the Earth: we see it as curved but thin enough so that locally, it can be treated as flat. In most all climate models, the 3D grid composing the atmosphere is tied to a 2D flat surface grid whose shape and area extends through the atmospheric layers to a subjective top-of-atmosphere height, typically 80 km for climate modeling. A simple picture of the spherical atmosphere and its flattened form is shown in Fig. 1. These 2 atmospheres are fundamentally different in how they intercept sunlight, and we identify 2 distinct factors: the light path and the spherical geometric expansion.

The light path is the most obvious error in the flat atmosphere and centers on the distortion of a straight line under the spherical-to-flat coordinate transformation. In Fig. 1A, the ray-tracing back to the sun at a surface solar zenith angle (SZA) of 88° is shown by the straight red lines originating at each layer. Here we assume parallel solar rays, ignoring sphericity associated with the sun–Earth distance (corrections are an order of magnitude smaller). The true light path ray traces in a flat atmosphere (Fig. 1B) appear as curves, reducing the zenith angle through each successive layer. The consequence of this is that the air mass factor, the ratio of path length to layer thickness, becomes smaller with altitude. In the flat atmosphere model where the air mass factors are constant, there is an exaggerated absorption of sunlight in the upper atmosphere, heating the upper atmosphere disproportionately relative to the lower.

Another aspect of the spherical light path is twilight. After the sun sets, we see the atmosphere overhead as sunlit. For example, when the sun is 4° below the horizon at the surface, the stratosphere is fully sunlit in clear skies with solar heating and active photochemistry, including Antarctic ozone depletion (1, 2). Thus, most atmospheric chemistry models use spherical solar ray tracing (3, 4), while most climate and Earth system models have retained the flat Earth ray tracing where atmospheric heating stops at an SZA of 90° . Several climate models

use a curvature correction to SZA that limits the air mass factor ($1/\cos(\text{SZA})$ in a flat atmosphere) approaching sunset but still treat the atmosphere as flat (Fig. 1B) and shut off the sun for $\text{SZA} \geq 90^\circ$ (5–7). The light paths in a spherical atmosphere can be simplified as straight lines (3) or can bend to include refraction (8, 9) (*Methods*). Flat atmospheres can include refraction, but at most this is invoked as a maximum air mass factor as SZA approaches 90° , which is still held constant through altitude.

In flat Earth models a column atmosphere is a polygonal cylinder with the same area A_0 from the surface to the top of atmosphere, while in a spherical atmosphere the columnar area expands like a cone as $A_0(1 + Z/R)^2$, with Z being the geometric height above the surface at radius R . Thus, a flat climate model is missing part of the climate system. The flat model solves the 1D planar hydrostatic equation with the gravitational acceleration fixed at its surface value $g_0 \sim 9.81 \text{ m}\cdot\text{s}^{-2}$. The mass of a layer in a flat column atmosphere with surface area A_0 is

$$dM_{\text{flat}} = A_0 dP / g_0 = -\rho(P) A_0 dZ_{\text{pot}}, \quad [1]$$

where P is pressure, ρ is density, and Z_{pot} is the geopotential height used in flat atmosphere models. Assuming a known profile of $T(P)$ and composition as a function of P , then the profile of $\rho(P, T)$ is also known. The profile $Z(P)$ is integrated with the hydrostatic equation (right 2 terms in Eq. 1), again assuming that the gravitational acceleration $g(Z)$ is a constant g_0 . The thickness of a layer in the flat geopotential atmosphere is less than that in

Significance

Early climate and weather models, constrained by computing resources, made numerical approximations on modeling the real world. One process, the radiative transfer of sunlight through the atmosphere, has always been a costly component. As computational ability expanded, these models added resolution, processes, and numerical methods to reduce errors and become the Earth system models that we use today. While many of the original approximations have since been improved, one—that the Earth's surface and atmosphere are locally flat—remains in current models. Correcting from flat to spherical atmospheres leads to regionally differential solar heating at rates comparable to the climate forcing by greenhouse gases and aerosols. In addition, spherical atmospheres change how we evaluate the aerosol direct radiative forcing.

Author contributions: M.J.P. designed research; M.J.P. and J.C.H. performed research; M.J.P. and J.C.H. analyzed data; and M.J.P. and J.C.H. wrote the paper.

The authors declare no conflict of interest.

This article is a PNAS Direct Submission.

This open access article is distributed under Creative Commons Attribution-NonCommercial-NoDerivatives License 4.0 (CC BY-NC-ND).

¹M.J.P. and J.C.H. contributed equally to this work.

²To whom correspondence may be addressed. Email: mprather@uci.edu.

This article contains supporting information online at www.pnas.org/lookup/suppl/doi:10.1073/pnas.1908198116/-DCSupplemental.

First published September 9, 2019.

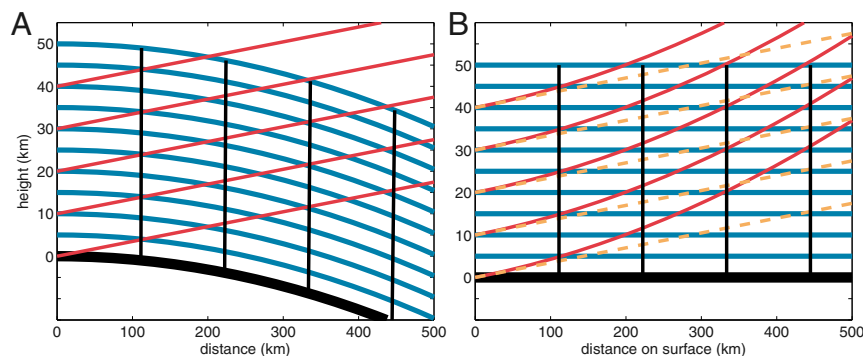


Fig. 1. Height (km) by distance (km) plot of surface (thick black line) and atmospheric layers (blue, every 5 km in height). (A) Spherical Earth and (B) flat Earth grid as used by most climate or Earth system models. The solid red lines show straight, unrefracted ray traces back to the sun for a SZA of 88°, which are (A) straight lines and (B) curved lines in the flat Earth grid. The dashed orange lines in B show the assumed ray trace to the sun in flat Earth models. For perspective on the curvature of the Earth, thin black lines demark 1° grid cells in the atmosphere: in A these are radial lines, and in B they are parallel lines. While not readily apparent on this scale, the length of the arc is 111 km at the surface and 112 km at 50 km height. We adopt the authalic radius of 6,371.0 km to ensure the same surface area as that of the true ellipsoidal Earth.

the true geometric spherical atmosphere because g does not decrease with height,

$$dZ_{\text{pot}} = dZ / (1 + Z/R)^2. \quad [2]$$

This geometric–geopotential effect is noted in the National Center for Atmospheric Research (NCAR) Whole Atmosphere Community Climate Model (WACCM), which uses fixed g_0 , but it is dismissed as a problem for analyzing model output (10).

The spherical hydrostatic equation for a radially symmetric atmospheric layer with the same dP and ρ includes both conic expansion of the column and the correct gravitational acceleration to give a layer mass of

$$\begin{aligned} dM_{\text{sphere}} &= (1 + Z/R)^2 A_0 dP / g(Z) = (1 + Z/R)^4 A_0 dP / g_0 \\ &= (1 + Z/R)^4 dM_{\text{flat}}. \end{aligned} \quad [3]$$

The spherical mass is greater than the flat mass by a factor of $1 + 4H/R$, where $H \sim 7$ km is the density scale height (see equation 12 in ref. 11 and also ref. 12). This extra 1/2% of the atmosphere is optically active and intercepts more sunlight, bringing additional energy to the surface and climate system. The additional mass increases from 0% at the surface to 5% at a height of 80 km, with about half occurring in the 0 to 12 km height range. It cannot be corrected by simply decreasing g_0 .

A survey has found effectively flat atmospheres for the following climate models: Goddard Space Flight Center (Goddard Earth Observing System Chemistry Climate Model [GEOSCCM] and Modern-Era Retrospective analysis for Research and Applications, version 2 [MERRA-2]) (13, 14), Goddard Institute for Space Studies 2E (15, 16), Department of Energy (Energy Exascale Earth System Model [E3SM]) (17, 18), Geophysical Fluid Dynamics Laboratory (Atmospheric Model version 3) (19, 20), NCAR WACCM (10), and European Centre for Medium-Range Weather Forecasts (ECMWF) Integrated Forecasting System (IFS) (6, 21, 22). Recent development in terms of solar radiation has focused on more accurate treatment of water vapor (23), fractional clouds (21, 24), and averaging over time steps (6) but ignores the spherical nature of the atmosphere (12, 25).

Correcting the optical mass from flat to spherical presents a conundrum. We can calculate the absorption of solar energy in the climate system more accurately, but the energy deposited in each layer will be inconsistent with the mass of that layer in the flat atmosphere, resulting in excessive local heating. Unfortunately,

the missing mass contributes to the heating of the climate system, including the surface. Here in Solar-J, we provide the capability for climate models to compute the scattering and absorption of sunlight in a spherical hydrostatic atmosphere that is consistent with their pressure and density profiles. It is up to the flat-atmosphere climate models to decide how to use this information.

When atmospheric layers expand with height, they increase the effective radius of the Earth in terms of capturing sunlight. For example, when calculating the sunlight incident on the climate system (i.e., stratosphere, troposphere, and surface; ozone, water vapor, aerosols, and clouds) with a refracting spherical expanded-mass atmosphere, we find about $2.5 \text{ W}\cdot\text{m}^{-2}$ more average radiation intercepted by the Earth than with a flat Earth model. If we include tropospheric aerosols and a large loading of stratospheric aerosols, the increase is about $3.2 \text{ W}\cdot\text{m}^{-2}$. This 0.7 to 1.0% increase is equivalent to extending the radius of the Earth by about 20 to 30 km. For example, even with clear-sky visible radiation, limb transmission of solar occultation measurements drops below 10% at 15 km height (26). This enhanced collection of sunlight is unevenly distributed geographically, however, with local increases of more than $10 \text{ W}\cdot\text{m}^{-2}$ in the twilight regions (7% of the globe at any given time). Photolysis rates that depend on overhead ozone column will increase at high SZA because of the reduced opacity of the spherical light path but will decrease at low SZA (high sun) because of the additional column mass using geometric heights. For example, at overhead sun, O_3 production from photolysis of O_2 in the lower stratosphere and upper tropical troposphere decreases by 4 to 6%, and excited atomic oxygen $\text{O}(^1\text{D})$ in the troposphere decreases by 1%.

Solar-J version 7.6c, presented here, offers 4 options: option 0, *flat*, uses the flat atmosphere optical mass in each layer with a fixed air mass fraction of $1/\cos(\text{SZA})$ and a rigid cutoff at 90° SZA (Fig. 1B); option 1, *sphr*, adds true straight-line light paths (Fig. 1A) assuming the geopotential height grid, allowing for twilight; option 2, *refr*, allows these light paths to refract, extending surface sunset to SZAs of $\sim 90.5^\circ$; and option 3, *geom*, assumes increased optical mass in spherically expanded layers on a geometric height grid with refracted light paths. The solar intensity and flux deposited in each atmosphere are calculated accurately for each of these 4 models. For multiple scattering and absorption of diffuse solar radiation, Solar-J adopts the pseudospherical approach (8, 27) in which the solar intensity and flux are used in a 1D plane-parallel multistream Feautrier code (3, 28). The net solar flux deposited in each layer is derived from the divergence of the diffuse flux plus the direct beam. When

invoking the spherical geometric atmosphere (*geom*), the direct beam's deposition is enhanced by a factor $(1 + Z/R)^2$ to account for the increase in atmospheric surface area. The increase in optical depth by the same factor due to the shift from geopotential to geometric heights has already been included in a corrected atmospheric profile of optical properties. These corrections for the 1D multiple-scattering ensure that all of the light scattered or absorbed within the expanding cone of atmospheric layers are included in that column's energy budget. We do not consider the next order of correction for true spherical multiple scattering (29).

Profiles of the solar intensity for SZA from 0° to 94° are shown in Fig. 2A for the 4 models (*flat*, *sphr*, *refr*, and *geom*). This calculation assumes clear-sky conditions in the visible (600 nm) where the only optical components are O_3 Chappuis absorption and molecular Rayleigh scattering. The *flat* model starts deviating from *sphr* by SZA = 60° , and at SZA = 88° , *flat* overlaps with the SZA = 90° profiles of *sphr*, *refr*, and *geom*. The refracting codes (*refr* and *geom*) show increased intensity below 20 km compared with the straight-line light path *sphr* code for SZA > 90° as expected. The *refr* and *geom* differences, due only to the shift to geometric altitude, are barely discernible. The inflection point about 24 km in the SZA = 92° profile results from the solar rays at their tangent point passing below the weakly absorbing ozone layer. Similarly, when there are sharp cloud layers in the troposphere, there is often a full reversal with higher intensities in the lower layers for SZA > 90° . When the tangent point drops below the cloudy layer, the air mass factor for the cloudy layer is reduced (Fig. 1A). Such cases point to the difficulty in defining the incident solar flux in a spherical atmosphere.

We define incident flux as that attenuated within the atmosphere or scattered by the surface. For a flat atmosphere, it is simply and always equal to $\cos(\text{SZA})$ times the solar flux. For a spherical atmosphere, it depends on the altitude and opacity of the atmosphere, and we show this in Fig. 2B for a case with 12-km-high cloud layer (optical depth = 4.2) and an aerosol-like layer in the lowest 5 km (optical depth = 0.08). Both cases use the same optical properties (liquid, stratus-like clouds) in an atmosphere with only weak Rayleigh scattering (800 nm). Both cloud layers (*sphr* = teal, *refr* = gray-green) and aerosol

layers (*sphr* = red, *refr* = gold) intercept more sunlight, increasing the incident flux, but they also shadow the surface, decreasing the incident flux. The total atmosphere, surface, and net changes are shown in Fig. 2B. In this case and in general, optically thin aerosol or cloud layers have a net positive incident flux with the atmospheric capture exceeding the surface decrease, while optically thick layers reduce the incident flux. Nevertheless, even with optically thick clouds, the reduced incident flux remains still greater than that of the flat atmosphere.

Calculations shown here of the Earth's solar radiation budget use the new Solar-J version 7.6c and meteorological data for January 2015 from the ECMWF OpenIFS system (cycle 38R1) (30, 31). We use 3-h averages for temperature, pressure, water vapor, ice-/liquid-water clouds on a $1.1^\circ \times 1.1^\circ \times 60$ -layer flat grid. Ozone is taken from a satellite climatology, and no aerosols are included in the base version. We integrate over 31 d with a 1-h time step. Increases in global incident solar radiation from successively implementing *sphr*, *refr*, and *geom* are +1.6, +1.9, and +2.5 $\text{W}\cdot\text{m}^{-2}$, respectively, and are shown in Fig. 3 as a function of latitude. For perspective, a dashed line in Fig. 3 shows 1% of the total incident flux in the flat atmosphere. Errors in the full *geom* case are >2 $\text{W}\cdot\text{m}^{-2}$ over the sunlit globe and exceed 4 $\text{W}\cdot\text{m}^{-2}$ in 2 bands about 66°S and 66°N . For *geom*, about 60% of the increase in incident solar flux is absorbed by the climate system; this is split equally between atmosphere and surface, and in the atmosphere it is split equally between stratosphere and troposphere. Thus, the flat Earth climate models underestimate solar heating of the climate system by 1.5 $\text{W}\cdot\text{m}^{-2}$. See Table 1. For perspective, this difference is comparable to the total anthropogenic effective radiative forcing over the industrial era of 2.3 $\text{W}\cdot\text{m}^{-2}$ (32), which has produced a discernible climate change (33). Our *geom* correction is unlikely to effect the modeled climate change from preindustrial to present day, but it will likely shift both reference climates by amounts similar to the climate change, thus altering the model skill in reproducing the current climate (34).

Working in spherical atmospheres causes us to reexamine how we calculate the radiative effect of aerosols on climate. As one test case, we use the NCAR monthly mean 3D tropospheric anthropogenic aerosol climatology for surface area active in heterogeneous chemistry (35). When converted to a mix of aerosol types, we calculate a global mean 600-nm optical depth of 0.088,

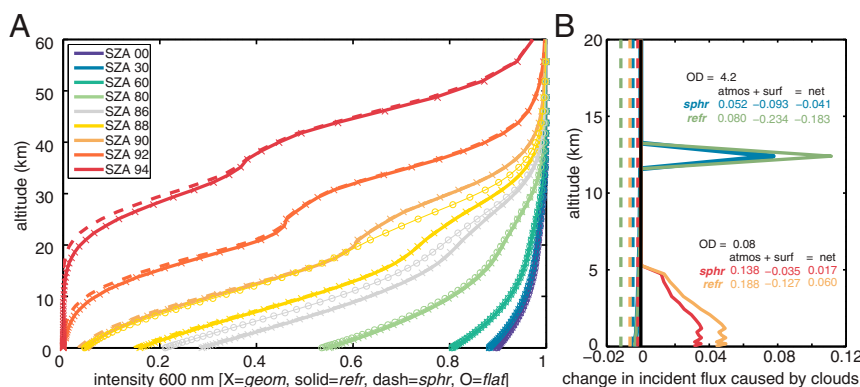


Fig. 2. (A) Altitude profiles of the clear-sky intensity of sunlight at 600 nm as a function of SZA. Results are shown for flat grid (circles, stop at 88°), spherical light paths (*sphr*, dashed lines), spherical plus refraction (*refr*, solid lines), and spherical plus refraction plus geometric affects (*geom*, crosses). The inflection in the profiles for large SZA is caused by the ozone layer absorption. Below 30 km altitude, the flat grid model at 88° overlaps with the spherical models at 90° , consistent with spherical corrections that freeze the zenith angle at 88.6° until flat Earth sunset (6) (B) Relative change in incident solar flux at SZA = 88° caused by a 12-km liquid water cloud of OD = 4.2 (2 green colors) and by 0 to 5 km aerosol layer of OD = 0.08 (2 red-orange colors). Results are shown only for *sphr* (darker colors) and *refr* (lighter colors); effects of *geom* are small here. Change is relative to the clear-sky model for that light path assumption. The quantity plotted is change per kilometer so that the area under each curve is a measure of the total. The negative incident flux at the surface is plotted here (dashed lines) as if averaged over 20 km so that it can be compared with the solid curves. The summed net change in incident flux for atmosphere and surface is given. Optically thick clouds tend to have less incident flux than clear sky because of the great reduction of incident flux at the surface, while optically thin aerosol-like cloud tend to increase the incident flux. In all cases the total incident flux is greater than that of the flat grid model.

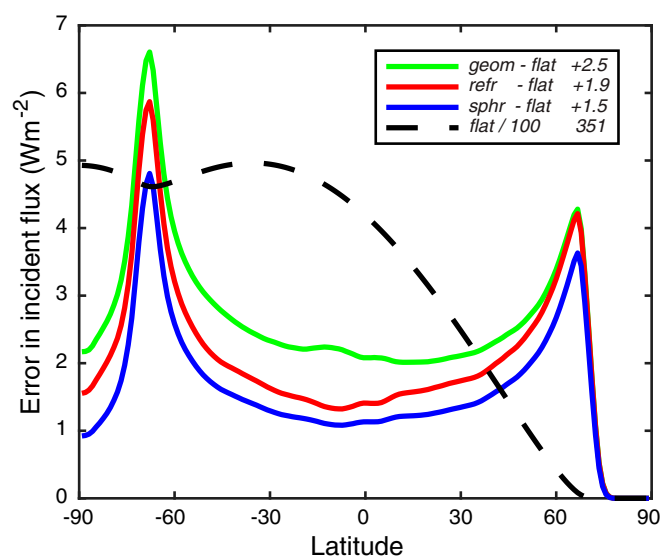


Fig. 3. Increase in incident solar flux ($\text{W}\cdot\text{m}^{-2}$) relative to a flat Earth model as a function of latitude averaged over January 2015. Results are from a full solar heating code (24) updated to include the light path and geometric effects described here: *sphr* (blue), *refr* (red), and *geom* (green). See Table 1 notes, text, and *SI Appendix*. About 60% of the increase in incident solar flux is absorbed by the climate system, and 40% is reflected. The total incident flat Earth flux, scaled by a factor of 1/100, is plotted as a function of latitude (black dashed).

typical of others (36). For January we calculate the aerosol direct radiative forcing (also known as instantaneous radiative effect). Our aerosols increase reflected sunlight by $1.56 \text{ W}\cdot\text{m}^{-2}$, but they reduce the total heating by only $1.35 \text{ W}\cdot\text{m}^{-2}$ because they catch more sunlight, increasing the incident flux by $0.21 \text{ W}\cdot\text{m}^{-2}$ (Table 2). The balance between atmospheric heating and surface cooling here is similar to recent model comparisons (37), and we find that the flat atmosphere high-bias errors of about 7% are comparable to the identified model errors (figure 2 of ref. 37). In another test case, we take the stratospheric aerosol loading and effective radius from the geoengineering model intercomparison project (38, 39). Our 600-nm optical depth of about 0.094 is similar to other models in the project and also to the levels following large volcanic eruptions. For stratospheric sulfate aerosols, our test is more rigorous because we can accurately calculate and resolve their optical properties and effects through 1) the index of refraction for

different weight percent solutions of sulfuric acid, 2) Mie scattering, and 3) 8-stream multiple scattering. The geoengineered cooling derived from the increase in reflected sunlight, $-2.8 \text{ W}\cdot\text{m}^{-2}$, must be offset by the increase in incident flux, $+0.5 \text{ W}\cdot\text{m}^{-2}$. Thus we need to evaluate aerosol–climate effects in terms of the change in heating of the climate system rather than by the change in reflected solar energy.

Conclusions

The approach here is only an approximation to radiative transfer solutions for a spherical hydrostatic atmosphere, but it is a low-cost option to greatly improve the accuracy of photolysis, photosynthesis, and solar heating in current models. Calculation of the direct solar beam is rigorous. Reverting to a plane-parallel scattering code does not address the 3D nature of scattered light (e.g., sides of clouds (22) and shift in quadrature angles with altitude (Fig. 1)), but it is still an improvement over flat atmospheres. Implementing these spherical corrections within an existing flat solar heating code should be straightforward and without significant penalty on computational efficiency. In Solar-J, the ray tracing and geometric corrections are calculated once for each column atmosphere and SZA and then applied to all wavelengths and combinations of cloud cover. This is an approximation as refraction depends somewhat on wavelength and atmospheric scale height. The attenuation of solar flux uses the optical properties for each wavelength band and applies Beer's Law along each ray path to the sun. The solar intensity at each layer edge has a unique ray path and is not directly related to the intensity at the layer above. A possibly disruptive effect of spherical atmospheres is that a radiation call must be made for about 58% of the grid cells that are sunlit instead of exactly 50% and thus may affect load balancing. Most chemistry models have pseudospherical atmospheres with twilight photochemistry and have dealt with load balancing across column atmospheres.

Calculation of solar energy absorption in a spherical hydrostatic atmosphere like the Earth's using the *geom* option would seem to be the correct approach for climate modeling as the corrections relative to a flat, reduced mass atmosphere penetrate through the atmosphere to the ocean and land systems. Nevertheless, it raises questions of consistency and how to distribute the energy within the atmosphere.

Our results here are based on 1-h model stepping and produce the same magnitude wavenumber 24 oscillations in incident flux and atmospheric heating found previously (6, 40). Using a spherical atmosphere reduces the amplitude of both errors by about half because it softens the transition to dusk but does not eliminate the need for some approach to averaging the heating

Table 1. Global mean solar fluxes ($\text{W}\cdot\text{m}^{-2}$) for January 2015 with clouds, no aerosols

Model	Incident	Reflected	Absorbed	Atmosphere absorbed		
				Stratosphere	Troposphere	Surface absorbed
<i>flat</i>	351.43	111.72	239.71		76.47	163.23
				13.66	62.81	
Differences						
<i>sphr</i> – <i>flat</i>	+1.55	+0.68	+0.87	+0.46		+0.41
				+0.27	+0.19	
<i>refr</i> – <i>flat</i>	+1.94	+0.83	+1.11	+0.53		+0.58
				+0.28	+0.25	
<i>geom</i> – <i>flat</i>	+2.50	+1.02	+1.48	+0.86		+0.62
				+0.48	+0.37	

The 4 model options are indicated here as follows: option 0, *flat*, 1D planar flat atmosphere; option 1, *sphr*, spherically symmetric atmosphere with solar ray traces as straight, unrefracted lines; option 2, *refr*, spherically symmetric atmosphere with refracted solar ray traces; and option 3, *geom*, spherically symmetric atmosphere with geometrically expanding altitudes, area, and mass. Options 0, 1, and 2 use geopotential heights and constant area with height.

Table 2. Aerosol direct radiative forcing ($\text{W}\cdot\text{m}^{-2}$) including incident flux for January 2015 all-sky conditions

Radiation model	Incident	Reflected	Atmosphere absorption	Surface absorption	Net absorption
NCAR anthropogenic tropospheric aerosols ($\text{OD}_{600\text{nm}} = 0.088$)					
Flat	0.00	+1.45	+4.28	−5.73	−1.45
Spherical	+0.19	+1.56	+4.32	−5.69	−1.37
Refractive	+0.13	+1.54	+4.31	−5.72	−1.41
Geometric	+0.21	+1.56	+4.35	−5.70	−1.35
GeoMIP stratospheric sulfate aerosols ($\text{OD}_{600\text{nm}} = 0.094$)					
Flat	0.00	+2.54	−0.40	−2.13	−2.53
Spherical	+0.40	+2.78	−0.42	−1.97	−2.39
Refractive	+0.31	+2.75	−0.43	−2.00	−2.43
Geometric	+0.49	+2.85	−0.42	−1.93	−2.36

These calculations include clouds; a clear-sky calculation has $3\times$ the reflected energy, $\sim 4.6 \text{ W}\cdot\text{m}^{-2}$.

rates over the full time step at each longitude (6). In contrast with ref. 6, our code has no obvious bias in stratospheric heating rates because we do not alter the air mass factors approaching sunset: differences between 1-h and 30-min time steps is less than $0.001 \text{ K}\cdot\text{d}^{-1}$. The difference in stratospheric heating rates with sphericity is quite large, however: $+0.6 \text{ K}\cdot\text{d}^{-1}$ near the strato-pause in 2 bands about 66°S and 66°N .

Spherical atmospheres should also affect the thermal infrared cooling of the Earth. Effects would include the increase in overall opacity (thicker geometric layers) but also smaller opacity along nonzenith ray paths to space (air mass factors decrease with height along a ray path; Fig. 14). The sign of the bias is not obvious, but an investigation using the tools developed here could be readily made. For planets with atmospheric scale height to radius ratios greater than the Earth's ($\sim 0.1\%$), such as Venus or Mars ($\sim 0.3\%$), spherical and geometric effects will become more pronounced.

Without implementing these spherical corrections in a climate model, we can only speculate on how they would affect the simulated climate. Does an additional global $2 \text{ W}\cdot\text{m}^{-2}$ out of a total heating of $240 \text{ W}\cdot\text{m}^{-2}$ matter? Since climate models can clearly detect the climate change caused by similar levels of human forcing (41), the shift in climate caused by flat atmosphere errors should be obvious. Also, $2 \text{ W}\cdot\text{m}^{-2}$ is typical of the model-to-model differences in atmospheric heating (42). The spherical corrections, even for the flat atmosphere mass, are not uniform and thus may cause much larger corrections in the stratosphere and winter poles. The spherical photochemistry modules already being used in Earth system models can be merged with the solar heating modules to maintain physically consistent codes.

Methods

The solar heating rates calculated here use updated versions of the standalone Cloud-J code (43) and the Solar-J code (24) embedded within the University of California, Irvine, chemistry-transport model. This latter model was run for January 2015, taking hourly steps and using meteorological data from the ECMWF IFS forecasts at T159L60 resolution (about $1.1^\circ \times 1.1^\circ$ resolution with 60 layers; for details, see ref. 31). Ozone profiles are taken from a satellite climatology included in Cloud-J and Solar-J. Solar-J uses the superbins and water vapor subbin absorption of Rapid Radiative Transfer Model for shortwave radiation (RRTMG-SW) for wavelengths greater than 600 nm. Cloud-J includes the same superbins and cloud absorption as Solar-J but does not include water vapor absorption. The new versions 7.6c of both models in standalone forms are provided in ref. 44.

The stratospheric geoengineering sulfate aerosols are taken from The Geoengineering Model Intercomparison Project (GeoMIP) specification for experiment G4-SSA (38). Data are taken from the midscenario, near-steady-state values for zonal mean effective radius and H_2SO_4 density in the file: geomip_ccmi_2020-2071_volc_v3.nc, from the GeoMIP website. The density was converted into a more general form of mass ratio ($\text{kg H}_2\text{SO}_4$ per kg air)

and scaled up to include the 25 wt % of H_2O in the aerosols. The first 8 terms of the scattering phase function, the single scattering albedo, and the extinction efficiency (often denoted by Q) were calculated with a Mie code assuming a refractive index for 75 wt % sulfuric acid aerosols (density = $1.746 \text{ g}\cdot\text{cm}^{-3}$), which is typical for the stratospheric sulfate layer. The aerosol size distribution was assumed to be log-normal with a width of 1.25. Separate calculations for the 27 wavelength bins of Solar-J were made for effective radius of 0.02, 0.04, 0.08, 0.10, 0.14, 0.20, 0.30, 0.50, 0.75, 1.0, 1.2, 1.4, 2.0, 3.0, and 5.0 microns. For the GeoMIP aerosols, we selected the optical properties from the one of these 15 precalculated size bins with the effective radius closest to that prescribed in the layer. We calculate an annual mean sulfur loading of 2.08 TgS, consistent with the GeoMIP documentation (38). For January 2015, we have a mean optical depth at 600 nm of 0.0935. GeoMIP also causes photochemical perturbations. In the lower stratosphere, O_3 production from photolysis of O_2 decreases by 2 to 3% while atomic O increases by 1 to 4%, thus generating a direct photochemical depletion of ozone independent of heterogeneous chemistry. In the tropospheric boundary layer, $\text{O}(^1\text{D})$ decreases by 1.3% reducing hydroxyl radical (OH) concentrations, but this does not include the expected decreases in stratospheric ozone. For this GeoMIP calculation, we believe our direct radiative results to be accurate, more so than most of the radiation codes used in the GeoMIP models: the optical properties are based directly on the refractive index for sulfuric acid–water mixtures and averaged over the wavelength bins, we include the wt % of H_2O , and the multiple scattering solution uses 8-streams for the diffuse radiation with no equivalent-isotropic reduction in optical depth.

The tropospheric aerosols are taken from 3D monthly mean, 10-y averages of surface area densities (μm^2 per cm^3) from the Community Earth System Model version 1.2 (35) supplied by S. Tilmes on 17 February 2016. The surface area includes the wet radius. Being intended for heterogeneous surface chemistry, it does not include sea salt, dust, or specific hydrophobic aerosols but is primarily biomass burning aerosols, industrial sulfate, and other hydrophilic aerosols. For optical properties, we split the surface area into 2 types: 1) combustion aerosol with effective radius of $0.14 \mu\text{m}$, single scattering albedo at 600 nm = 0.89, and extinction efficiency at 600 nm $Q = 1.06$ and 2) dust aerosol with effective radius of $0.15 \mu\text{m}$, single scattering albedo = 0.98, and extinction efficiency $Q = 1.28$. These 2 were chosen because they are available as standard aerosol types in Fast-J (#9 and #11, respectively) and they give typical values for overall single scattering albedo, Angstrom coefficient, and optical depth at 600 nm of 0.0877. We recognize that dust aerosol was not included as anthropogenic aerosol in the CESM data. In this paper, the tropospheric aerosol loading is chosen as a didactic example for anthropogenic aerosols, to demonstrate the role of spherical atmospheres. A more accurate evaluation of the direct radiative forcing of tropospheric aerosols would have to include the full range of anthropogenic aerosol optical types and sizes.

The treatment of air mass factors in a spherical refracting atmosphere are described in the equations A.1–A.34 of *SI Appendix*. The radiative transfer solution is done for each grid cell column atmosphere, assuming that it is horizontally homogeneous in spherical shells. The unrefracted SZA for each column atmosphere is the same at each layer edge throughout the column and is determined by latitude, longitude, solar declination, and local time. With refraction, the zenith angle of the refracted beam is reduced relative to that of the unrefracted solar beam, in proportion to vertical gradients in

density. We adopt 1.00030 as the index of refraction of air for all wavelengths at the surface with a fixed density scale height of 8 km. This assumption can be revised to include realistic density variations and wavelength dependence of the refractive index (e.g., from 1.00030 in the UV to 1.00027 in the near infrared). Presently, Solar-J is designed for the stratosphere and troposphere, and thus, we shut off the heating rate calculation for SZAs greater than 98°, corresponding to no direct solar beam below 62 km.

The absorption and extinction of the direct solar rays are calculated with correct spherical geometry, using geopotential (*sphr* and *refr*) and geometric (*geom*) heights. This calculation provides the solar source terms for the scattering calculation, for which we revert to our plane-parallel (flat atmosphere), multiple-scattering code (3), increasing the optical mass of the flat atmosphere layer in the *geom* option to account for the additional thickness and areal extent of the layer. This method of combining spherically

calculated direct solar terms with a 1D plane-parallel model for the diffuse solar radiation provides a reasonable approximation to spherical atmosphere that is exact in limiting cases such as optically thin layers.

The standalone codes for Solar-J and Cloud-J versions 7.6c, along with other data in the paper are published with University of California, Irvine Dash (44).

ACKNOWLEDGMENTS. This work was developed with support from the US Department of Energy, Office of Science, Biological and Environmental Research Program (award DE-SC0012536); Lawrence Livermore National Laboratory (subcontract B628407) under the E3SM project; and the NASA Modeling, Analysis and Prediction program (award NNX13AL12G). We greatly appreciate the efforts of Tim Cronin and the anonymous reviewers for improving the overall presentation and identifying our inconsistent treatment of the spherical hydrostatic atmosphere, which is now corrected.

- D. E. Anderson, S. E. Lloyd, Polar twilight UV-visible radiation field: Perturbations due to multiple scattering, ozone depletion, stratospheric clouds, and surface albedo. *J. Geophys. Res.* **95**, 7429–7434 (1990).
- S. Solomon, R. W. Sanders, H. L. Miller, Jr, Visible and near-ultraviolet spectroscopy at McMurdo Station, Antarctica 7. OClO diurnal photochemistry and implications for ozone destruction. *J. Geophys. Res.* **95**, 13807–13817 (1990).
- O. Wild, X. Zhu, M. J. Prather, Fast-J: Accurate simulation of in- and below-cloud photolysis in tropospheric chemical models. *J. Atmos. Chem.* **37**, 245–282 (2000).
- X. X. Tie *et al.*, Effect of clouds on photolysis and oxidants in the troposphere. *J. Geophys. Res.* **108**, 4642 (2003).
- A. A. Lacis, V. Oinas, A description of the correlated kappa-distribution method for modeling nongray gaseous absorption, thermal emission, and multiple-scattering in vertically inhomogeneous atmospheres. *J. Geophys. Res.* **96**, 9027–9063 (1991).
- R. J. Hogan, S. Hirahara, Effect of solar zenith angle specification in models on mean shortwave fluxes and stratospheric temperatures. *Geophys. Res. Lett.* **43**, 482–488 (2016).
- G. W. Paltridge, C. M. R. Platt, *Radiative Processes in Meteorology and Climatology, Developments in Atmospheric Science* (Elsevier Scientific Pub. Co., Amsterdam, 1976), 318 p.
- V. V. Rozanov, M. Buchwitz, K. U. Eichmann, R. de Beek, J. P. Burrows, SCIATRAN—A new radiative transfer model for geophysical applications in the 240–2400 nm spectral region: The pseudo-spherical version. *Adv. Space Res.* **29**, 1831–1835 (2002).
- D. A. Thompson, T. J. Pepin, F. W. Simon, Ray tracing in a refracting spherically symmetric atmosphere. *J. Opt. Soc. Am.* **72**, 1498–1501 (1982).
- H.-L. Liu *et al.*, Development and validation of the Whole Atmosphere Community Climate Model with thermosphere and ionosphere extension (WACCM-X 2.0). *J. Adv. Model. Earth Syst.* **10**, 381–402 (2018).
- K. E. Trenberth, C. J. Guillemot, The total mass of the atmosphere. *J. Geophys. Res.* **99**, 23079–23088 (1994).
- M. H. P. Ambaum, General relationships between pressure, weight and mass of a hydrostatic fluid. *Proc. R. Soc. A* **464**, 943–950 (2008).
- M. D. Chou, A solar-radiation model for use in climate studies. *J. Atmos. Sci.* **49**, 762–772 (1992).
- A. Molod *et al.*, “The GEOS-5 atmospheric general circulation model: Mean climate and development from MERRA to Fortuna” in *Technical Report Series on Global Modeling and Data Assimilation*, M. J. Suarez, Ed. (National Aeronautics and Space Administration, 2012), vol. 28, pp. 117.
- V. Oinas, A. A. Lacis, D. Rind, D. T. Shindell, J. E. Hansen, Radiative cooling by stratospheric water vapor: Big differences in GCM results. *Geophys. Res. Lett.* **28**, 2791–2794 (2001).
- G. A. Schmidt *et al.*, Configuration and assessment of the GISS ModelE2 contributions to the CMIP5 archive. *J. Adv. Model. Earth Syst.* **6**, 141–184 (2014).
- J. C. Golaz *et al.*, The DOE E3SM coupled model version 1: Overview and evaluation at standard resolution. *J. Adv. Model. Earth Syst.* **11**, 2089–2129 (2019).
- H. W. Barker *et al.*, The Monte Carlo independent column approximation: An assessment using several global atmospheric models. *Q. J. R. Meteorol. Soc.* **134**, 1463–1478 (2008).
- S. M. Freidenreich, V. Ramaswamy, A new multiple-band solar radiative parameterization for general circulation models. *J. Geophys. Res.* **104**, 31389–31409 (1999).
- M. Zhao *et al.*, The GFDL global atmosphere and land model AM4.0/LM4.0: 2. Model description, sensitivity studies, and tuning strategies. *J. Adv. Model. Earth Syst.* **10**, 735–769 (2018).
- J. J. Morcrette, H. W. Barker, J. N. S. Cole, M. J. Iacono, R. Pincus, Impact of a new radiation package, McRad, in the ECMWF integrated forecasting system. *Mon. Weather Rev.* **136**, 4773–4798 (2008).
- R. J. Hogan, A. Bozzo, A flexible and efficient radiation scheme for the ECMWF model. *J. Adv. Model. Earth Syst.* **10**, 1990–2008 (2018).
- R. Pincus, B. Stevens, Paths to accuracy for radiation parameterizations in atmospheric models. *J. Adv. Model. Earth Syst.* **5**, 225–233 (2013).
- J. Hsu, M. J. Prather, P. Cameron-Smith, A. Veidenbaum, A. Nicolau, A radiative transfer module for calculating photolysis rates and solar heating in climate models: Solar-J v7.5. *Geosci. Model Dev.* **10**, 2525–2545 (2017).
- K. E. Trenberth, L. Smith, The mass of the atmosphere: A constraint on global analyses. *J. Clim.* **18**, 864–875 (2005).
- W. P. Chu, M. P. McCormick, Inversion of stratospheric aerosol and gaseous constituents from spacecraft solar extinction data in the 0.38–1.0-microm wavelength region. *Appl. Opt.* **18**, 1404–1413 (1979).
- R. J. D. Spurr, VLIDORT: A linearized pseudo-spherical vector discrete ordinate radiative transfer code for forward model and retrieval studies in multilayer multiple scattering media. *J. Quant. Spectrosc. Radiat. Transfer* **102**, 316–342 (2006).
- P. Feautrier, Sur la resolution numerique de lequation de transfert. *C. R. Hebd. Acad. Sci.* **258**, 3189 (1964).
- R. D. M. Garcia, A P-N particular solution for the radiative transfer equation in spherical geometry. *J. Quant. Spectrosc. Radiat. Transfer* **196**, 155–158 (2017).
- G. Szépszó, V. Sinclair, G. Carver, Using the ECMWF OpenIFS model and state-of-the-art training techniques in meteorological education. *Adv. Sci. Res.* **16**, 39–47 (2019).
- M. J. Prather *et al.*, Global atmospheric chemistry—Which air matters. *Atmos. Chem. Phys.* **17**, 9081–9102 (2017).
- G. Myhre *et al.*, “Anthropogenic and natural radiative forcing” in *Climate Change 2013: The Physical Science Basis, IPCC WGI Contribution to the Fifth Assessment Report*, T. F. Stocker, *et al.*, Eds. (Cambridge University Press, Cambridge, United Kingdom, 2013), chap. 8, pp. 659–740.
- IPCC, “Summary for policymakers” in *Climate Change 2013: The Physical Science Basis. Contribution of Working Group I to the Fifth Assessment Report of the Intergovernmental Panel on Climate Change*, T. F. Stocker, *et al.*, Eds. (Cambridge University Press, Cambridge, United Kingdom, 2013), chap. SPM, pp. 1–30.
- G. Flato *et al.*, “Evaluation of climate models” in *Climate Change 2013: The Physical Science Basis*, T. F. Stocker *et al.*, Eds. (Cambridge University Press, Cambridge, United Kingdom, 2013), chap. 9, pp. 741–866.
- S. Tilmes *et al.*, Description and evaluation of tropospheric chemistry and aerosols in the Community Earth System Model (CESM1.2). *Geosci. Model Dev.* **8**, 1395–1426 (2015).
- M. Chin *et al.*, Tropospheric aerosol optical thickness from the GOCART model and comparisons with satellite and Sun photometer measurements. *J. Atmos. Sci.* **59**, 461–483 (2002).
- A. L. Jones *et al.*, A new paradigm for diagnosing contributions to model aerosol forcing error. *Geophys. Res. Lett.* **44**, 12004–12012 (2017).
- S. Tilmes *et al.*, A new Geoengineering Model Intercomparison Project (GeoMIP) experiment designed for climate and chemistry models. *Geosci. Model Dev.* **8**, 43–49 (2015).
- B. Kravitz *et al.*, The geoengineering model intercomparison project phase 6 (GeoMIP6): Simulation design and preliminary results. *Geosci. Model Dev.* **8**, 3379–3392 (2015).
- L. J. Zhou, M. H. Zhang, Q. Bao, Y. M. Liu, On the incident solar radiation in CMIP5 models. *Geophys. Res. Lett.* **42**, 1930–1935 (2015).
- N. L. Bindoff *et al.*, “Detection and attribution of climate change: From global to regional” in *Climate Change 2013: The Physical Science Basis*, T. F. Stocker *et al.*, Eds. (Cambridge University Press, Cambridge, United Kingdom, 2013), chap. 10, pp. 867–952.
- M. Wild *et al.*, The global energy balance from a surface perspective. *Clim. Dyn.* **40**, 3107–3134 (2013).
- M. J. Prather, Photolysis rates in correlated overlapping cloud fields: Cloud-J 7.3c. *Geosci. Model Dev.* **8**, 2587–2595 (2015).
- M. Prather, J. Hsu, Solar-J and Cloud-J models version 7.6c, v2. University of California, Irvine Dash, Dataset. <https://doi.org/10.7280/D1096P>. Accessed 19 August 2019.

A round Earth for climate models

5 Michael J. Prather and Juno C. Hsu
Earth System Science Department, UC Irvine

Supporting Information Appendix

10 Our new method in Cloud-J and Solar-J versions 7.6c for determining the extinction of the direct solar beam as well as calculating the incident flux and the scattered diffuse flux are described here. A model with M layers, designated $K = 1:M$, has $M+1$ layer edges, designated $L = 1:M+1$. Each layer K is assumed to be uniform and defined by density, temperature, composition, and for
15 this paper, optical depth, single scattering albedo, and scattering phase function. Each layer edge L is defined by pressure. The layer edge altitude, Z_L , is calculated from the hydrostatic equation starting with the surface altitude Z_1 . Each layer edge has a radius R_L from the center of the Earth given by $R + Z_L$. For model options '*flat*', '*sphr*' and '*refr*', we use the flat-atmosphere 1D
20 hydrostatic equation with constant g_0 , and hence all altitudes are geopotential height. For option '*geom*', we use a spherical hydrostatic atmosphere with decreasing $g(Z) = g_0/(1 + Z/R)^2$ to get true geometric altitudes, which we designate Z^{geom} .

For a grid-cell column atmosphere (CA), the solar zenith angle A_{CA} used to start the ray trace is the same at each layer edge. Without refraction, all solar ray paths through the atmosphere are
25 straight lines. The invariant quantity along ray paths for column atmospheres on the sunlit side ($A_{CA} \leq 90^\circ$) that terminate at layer edge 1 is then:

$$\sin(A_L) R_L = \sin(A_{CA}) R_1 = \text{constant} \quad (\text{A.1})$$

This means that the apparent zenith angle of the sun at the top of the atmosphere is

$$\sin(A_{M+1}) = \sin(A_{CA}) R_1 / R_{M+1}. \quad (\text{A.2})$$

30 Given that $R_1 < R_{M+1}$, then $A_{M+1} \leq A_{CA}$ and the sun is more overhead (less attenuated) at higher altitudes (except for the special case $A_{CA} = 0^\circ$). Integrating from the top down to the surface, we can calculate the sequence of zenith angles A_K at radius R_K . The length from R_{K+1} to R_K along the solar ray path is the leg of the triangle connecting the radius vector R_{K+1} with the vector R_K , and is given by simple trigonometry as

$$35 \quad P(1, K) = R_{K+1} \cos(A_{K+1}) - R_K \cos(A_K). \quad (\text{A.3})$$

We define path length $P(L, K)$ as the distance through layer K of the solar ray ending at radius R_L . Note that starting at R_2 gives a different ray-path with invariant $\sin(A_{CA}) R_2$. On the sunlit side only overhead layers fall in the ray path,

$$40 \quad P(L, K) > 0 \text{ for } K=L:M, \text{ and } P(L, K) = 0 \text{ for } K=1:L-1. \quad (\text{A.4})$$

By definition $P(M+1, K) = 0$ for all K because at R_{M+1} (top of atmosphere) the solar ray does not pass through the atmosphere and is not attenuated. Note that this ray tracing involves path lengths through layers that are increasingly separated from the CA radius vector at angle A_{CA} , and thus in a 3D atmospheric model might belong to neighboring CAs.

45 When $A_{CA} > 90^\circ$, $\cos(A_{CA}) < 0$, and without refraction the surface is dark, and $P(1, K) \equiv 0$ for $K=1:M$. This condition, $P(L, K) \equiv 0$, holds until searching upward, we reach the first layer edge

$L > 1$ such that the ray path is no longer shadowed by the surface. In effect, the tangent radius, $\sin(A_{CA}) R_L$, is greater than R_1 . Starting at R_L , we follow the ray path downward through layer $L-1$ below, intersecting R_{L-1} at angle:

$$\sin(A_{L-1}) = \sin(A_{CA}) R_L / R_{L-1}. \quad (A.5)$$

Note that when calculating A_{L-1} from the sine, one must use the value $>90^\circ$ to ensure that the cosine remains negative. The path length through this layer, remembering that both cosines are negative, is then:

$$P(L, L-1) = \cos(A_{L-1}) R_{L-1} - \cos(A_L) R_L. \quad (A.6)$$

This process continues, following the ray path that started at R_L with $A_L = A_{CA}$, calculating $P(L, L-2)$ and so on, until radius R_J , where the ray path no longer hits a lower radius, but cuts a chord through the layer below, intersecting R_J on the sunlit side. This condition is

$$\sin(A_J) R_J > R_{J-1}. \quad (A.7)$$

The path through layer $J-1$ is the length of the chord:

$$P(L, J-1) = -2 \cos(A_J) R_J. \quad (A.8)$$

Starting at the radius R_J on the sunlit side, we reflect the zenith angle, $A_J' = 180^\circ - A_J < 90^\circ$, so that the cosine flips sign, and proceed upward as before. The path lengths $P(L, K=J:L-1)$ will have two separate parts, one from the dark side and one from the sunlit side; however both are equal in length for unrefracted paths. The path length P is converted to the dimensionless air mass factor by dividing by the thickness of layer K :

$$AMF(L, K) = P(L, K) / (R_{K+1} - R_K) \quad (A.9)$$

AMF is used in the radiative transfer solution to scale the optical depth of each layer in determining the extinction of sunlight along the path. The effective $\cos(A)$ in layer K for the path to radius L is $1/AMF(L, K) \leq 1$. Along a ray path, AMF changes with altitude, becoming smaller at higher altitudes. AMF is used to calculate the incident solar angle for the scattering phase function of the sun and the scale factor for the solar flux deposited in that layer. Calculations denoted here as '*sphr*' use only these corrections to the flat atmosphere.

With refraction the solar ray bends as it traverses layers of differing refractive index, and thus the refracted angle across each layer edge depends directly on density and somewhat on wavelength (1, 30). For a refracting atmosphere with index of refraction N_L in layer L with lower edge R_L , the invariant quantity along the ray path intersecting the surface R_1 at zenith angle A_1 is:

$$\sin(A_L) R_L N_L = \sin(A_1) R_1 N_1. \quad (A.10)$$

The refractive index in a vacuum is 1 and increases with density:

$$1 = N_{M+1} < N_M < \dots < N_1. \quad (A.11)$$

Due to refraction, the angle A_1 will not equal the CA zenith angle A_{CA} . A ray path bends toward the surface rather than traveling in a straight line, and there is no simple formula to find A_1 as a function of A_{CA} . For visible wavelengths in the Earth's atmosphere, $A_{CA} \sim 90^\circ$ results in $A_1 \sim 89.5^\circ$, i.e., when standing at the geometric terminator, the sun appears elevated 0.5° above the horizon.

The method of calculating the refractive path here involves iteration for ray paths that intersect the surface or interpolation across refracted paths that do not touch the surface. This method results in the surface being directly sunlit at $A_{CA} \sim 90.5^\circ$ and the apparent zenith angle being elevated (smaller path length) compared with the non-refracted atmosphere. This method is flexible for different profiles of N_L , but the accuracy depends on the number of layers per atmospheric scale height.

For $A_{CA} \leq 90^\circ$ we first ignore the elevation angle at radius R_L ($L=1:M$) and start integrating from the top of the atmosphere approximating the refracted invariant beginning at L with the constant:

$$sARN_L \equiv \sin(A_{CA}) R_L N_L \quad (A.12)$$

The zenith angle at the top of the atmosphere is:

$$\sin(A_{M+1}) = sARN_L / R_{M+1}. \quad (A.13)$$

The ray path bends as it reaches R_M and has zenith angle:

$$\sin(A_M) = sARN_L / (R_M N_M). \quad (A.14)$$

In order to calculate the elevation angle we need the angle between the two radius vectors R_{M+1} and R_M . The straight ray path upward from R_M at angle A_M intersects R_{M+1} at angle A'_M , which is given from the non-refracted invariant:

$$\sin(A'_M) R_{M+1} = \sin(A_M) R_M. \quad (A.15)$$

Thus, the zenith angle of the radius vector to R_M is $A_{M+1} + (A_M - A'_M)$. This sequence is continued down to radius point L , where the refracted zenith angle is:

$$A^r_L = A_{M+1} + (A_M - A'_M) + \dots + (A_L - A'_L) > A_{CA}. \quad (A.16)$$

The elevation angle, $A^r_L - A_{CA}$, is proportional to $N_L - 1$. We reduce the zenith angle of the ray path at R_L to $A_{CA} - (A^r_L - A_{CA})$, and the refracted invariant at L is revised to

$$sARN_L^* \equiv \sin(2 A_{CA} - A^r_L) R_L N_L \quad (A.17)$$

Using this new invariant, the process is repeated, now saving the path lengths:

$$P(L, M) = \cos(A'_M) R_{M+1} - \cos(A_M) R_M \quad (A.18)$$

and so forth down to $P(L, L)$. This procedure is repeated for $L = 1:M$. We iterate only once because elevation angles on the Earth are small, $<0.5^\circ$, but more iterations would increase the accuracy if needed.

For $A_{CA} > \sim 90.5^\circ$ we follow ray paths that bend around the Earth and continue through the post-terminator dark side to R_{M+1} without intersecting the surface. For this, we calculate and store the properties of all ray paths with tangent points at each radius R_L for $L=1:M$. The rays do not intersect and the refracted path from radius R_L at angle A_{CA} can be interpolated from the two tangent ray paths bounding that point. Starting with $L=1$, we calculate the refracted ray-path that is tangent to R_L . Due to refraction, this tangent point occurs at a zenith angle $A^{\tan}_L > 90^\circ$, which becomes closer and closer to 90° as L increases and N_L approaches 1. Because the path angle is tangent at R_L , the refracted invariant, $sARN_L$ is simply $R_L N_L$. We integrate starting at R_{M+1} (as above for $A_{CA} \leq 90^\circ$) along the sunlit side of the ray (superscript S), archiving the path lengths through each layer $P^{\tan S}$ and the zenith angles $A^{\tan S}$ where the refracted ray crosses each successive radius on the sunlit side:

$$\sin(A_{M+1}) = R_L N_L / R_{M+1} \quad (A.19)$$

$$\sin(A'_M) R_{M+1} = \sin(A_M) R_M$$

$$P^{\tan S}(L, M) = \cos(A'_M) R_{M+1} - \cos(A_M) R_M$$

$$A^{\tan S}(L, M) = A^r_M = A_{M+1} + (A_M - A'_M)$$

This continues down to the tangent point $A^{\tan S}(L, L) \equiv A^{\tan}_L > 90^\circ$. Note that $P^{\tan S}$ is a path length as is P , but the indexing is specific to tangent radii L , and we define $P^{\tan S}(L, J) = 0$ for $J < L$. For the angle $A^{\tan S}$, both indices are radius points and $A^{\tan S}(L, J)$ is undefined for $J < L$. The superscript S is used to denote the sunlit side of the ray path.

We can continue integrating from the tangent point out of the atmosphere up to R_{M+1} on the dark side, but the path can simply be reflected about the tangent point A^{\tan}_L without further

computation. The zenith angle at radius R_J on the dark side (superscript D) along this tangent path is reflected about A^{\tan}_L :

$$A^{\tan D}(L, J) = 2 A^{\tan}_L - A^{\tan S}(L, J) \text{ for } J=L:M. \quad (\text{A.20})$$

The post-terminator path lengths on the dark side $P^{\tan D}(L, J)$ are the same as $P^{\tan S}(L, J)$. With these matrices stored, we can interpolate the tangent ray path for an intermediate radius that passes through radius K in a column atmosphere at angle A_{CA} . From the interpolated values $P^{\tan S}(-, J)$ and $P^{\tan D}(-, J)$, we calculate a standard path $P(K, J)$:

$$\begin{aligned} P(K, J) &= P^{\tan S}(-, J) + P^{\tan D}(-, J) \text{ for } J < K; \\ &= P^{\tan S}(-, J) \text{ for } J \geq K. \end{aligned} \quad (\text{A.21})$$

We must calculate interpolated tangent ray paths, if they exist, for each radius in the CA in order to fill out the P matrix.

For a column atmosphere on the dark side with zenith angle $A_{CA} > A^{\tan}_1$ ($\sim 90.45^\circ$ for the Earth's atmosphere), the surface will be dark. $A^{\tan D}(1, J)$ is the zenith angle where the R_1 tangent path, exiting on the dark side, crosses R_J ; and thus for any column atmosphere where $A_{CA} \leq A^{\tan D}(1, J)$ R_J will be in direct sunlight. For each R_J in a given CA, we search upward from $L = 1$ (surface tangent ray) until we find a pair of tangent ray paths L and $L+1$ such that

$$A^{\tan D}(L+1, J) < A_{CA} \leq A^{\tan D}(L, J). \quad (\text{A.22})$$

We then interpolate linearly in angle A_{CA} between $P^{\tan S}(L+1, K)$ and $P^{\tan S}(L, K)$ to get the paths for the intermediate tangent ray $P^{\tan S}(-, K)$, and similarly for $P^{\tan D}(-, K)$, to get the standard path length $P(J, K)$ as noted above. For this dark side, $P(M+1, K=1:M)$ will have some non-zero values because the sunlight at the dark side radius $M+1$ is coming from below and must be attenuated through the atmosphere.

If the column atmosphere zenith angle lies in the middle zone for tangent ray at radius R_L , $90^\circ \leq A_{CA} < A^{\tan}_L$, then we cannot interpolate tangent paths. The ray path to R_L is wholly on the sunlit side since it occurs before the tangent point. We revert to direct integration following the sunlit path, but subtract the elevation angle at the tangent point ($A^{\tan}_L - 90^\circ$), and thus the invariant at end-point radius R_L used to start the integration of path lengths is

$$\sin(A_{CA} + 90^\circ - A^{\tan}_L) R_L N_L. \quad (\text{A.23})$$

The values for refraction used here are $N_1 = 1.00030$ and a density scale height of 8 km, so that $N_L = 1 + 0.00030 \exp[-(R_L - R_1)/8]$. In this model, we simplify the calculation of refraction so that the path lengths $P(L, K)$ apply to all wavelengths and are only calculated once for each CA and solar zenith angle. The value of N_1 scales with density and varies with wavelength from 1.00030 in the ultraviolet to 1.00027 in the near infrared. Presently, Solar-J is designed for the stratosphere and troposphere; and thus we shut off the heating rate calculation for solar zenith angles greater than 98° , corresponding to direct sunlight only above 62 km.

Although the generation of path lengths is complex with many conditionals, once defined, they allow us a straightforward coding for the solar intensity that is independent of wavelength bin.

We define a dimensionless air mass factor (AMF) from the path length and layer thickness

$$\text{AMF}(L, K) = P(L, K) / (Z_{K+1} - Z_K) \quad (\text{A.24})$$

For a given bin, the optical depth $d\text{TAU}$ in each layer K is a combination of absorption and scattering.

$$d\text{TAU}_K = d\text{TAU}_K^{\text{abs}} + d\text{TAU}_K^{\text{sca}} \quad (\text{A.25})$$

185 The total optical depth from layer edge L to the sun is simply the vector sum over all layers

$$\text{TTAU}^L = \sum_{K=1:M} [\text{AMF}(L, K) \text{ dTAU}_K] \quad (\text{A.26})$$
where $\text{AMF} = 0$ for layers that are not in the ray path. The intensity of sunlight is defined as 1 at the top of the atmosphere, and at layer edge L it is equal simply to

$$F_L = \exp[-\text{TTAU}^L]. \quad (\text{A.27})$$

190 Nominally, $F_{M+1} = 1$, but for post-terminator ray paths, and specifically $\text{AMF}(M+1, M) > 0$, the layer edge is lit from underneath and we use the formulae above.

The direct solar flux deposited in layer K, D_K , includes both absorbed and scattered components and counts as incident solar flux. D_K must be calculated carefully because heating rates are
195 calculated from the difference between D_K and the diffuse flux exiting the layer. In a flat atmosphere, this calculation is trivial: it is simply the difference in solar intensity between top and bottom of the layer divided by the AMF, where $1/\text{AMF}$ is simply $\cos(\text{SZA})$ throughout the atmosphere. The calculation of incident solar flux is more complex in a spherical atmosphere because the ray path at layer edge L goes through a different atmospheric path than that at L+1.
200 This is evident from the inflection point in solar intensity shown in Figure 2. We often see a reversal with $F_L > F_{L+1}$ as the ray path tangent drops below cloud or ozone layers. Thus, we calculate the incident flux in layer K from the upper and lower layer-edge solar intensities (F_{L+1} and F_L), scaling each by the optical properties in each half of the layer.

$$D_K = \frac{1}{2} (F_L + F_{L+1}) \text{ dTAU}_K^{\text{sca}} + ((1 - \exp[-\frac{1}{2} \text{ dTAU}_K^{\text{abs}} \text{ AMF}(K, K)]) F_{L+1} \\ + (\exp[+\frac{1}{2} \text{ dTAU}_K^{\text{abs}} \text{ AMF}(K, K)] - 1) F_L) / \text{AMF}(K, K) \quad (\text{A.28})$$

Note that deposition for scattering is linear because of the way scattering is calculated in the 1D plane parallel scattering model. For absorption, the deposition includes the attenuation of the upper intensity through half the layer and a reverse calculation of the attenuation that would have occurred to get the lower intensity. With this definition, the total incident flux exactly equals the
210 reflected plus absorbed at surface fluxes in a conservative scattering atmosphere. If there is direct sunlight at the surface, then the incident flux at the surface is simply

$$D_0 = F_1 / \text{AMF}(1, 1) \quad (\text{A.29})$$

Some care and reversal of exponential decay factors in A.28 is needed for post-terminator upward ray paths.

215 In a geometric spherical atmosphere, with effectively conic sections for each column atmosphere, the height of the atmospheric layers increase relative to the geopotential heights

$$Z_L^{\text{geom}} = Z_L^{\text{geop}} (1 + Z_L^{\text{geom}}/R) \quad (\text{A.30})$$

where we have assumed $Z_1 = 0$. Given that density vs. pressure profile is not changed, the mass
220 and optical depth in each layer also increases

$$\text{dTAU}_K^{\text{geom}} = \text{dTAU}_K^{\text{geop}} (1 + Z_K^{\text{geom}}/R)^2 \quad (\text{A.31})$$

where Z_K refers to the height at the middle of layer K. The solar-ray path lengths through each layer AMFs are calculated using the new Z_L^{geom} , and equations A.24-A.29 including AMFs and F_L are calculated using Z^{geom} and $\text{dTAU}^{\text{geom}}$.

225 The calculation of diffuse radiation reverts to our multiple-scattering, plane-parallel, flat-atmosphere code (3). In this calculation, the solar intensities at each layer edge (F_L) plus the optical depth (dSTAU_K) and intrinsic optical properties (single scattering albedo, scattering phase function) are used. For options *flat*, *sphr*, and *refr*, the calculated F_L specific to that option
230 is used along with

$$d\text{STAU}_K = d\text{TAU}_K^{\text{geop}}. \quad (\text{A.32})$$

For option *geom*, we must further increase the optical depth due to the areal expansion, effectively pulling all of the optical mass into a column with the area of the surface grid.

$$d\text{STAU}_K = d\text{TAU}_K^{\text{geom}} (1 + Z_K^{\text{geom}}/R)^2 \quad (\text{A.33})$$

235 With this increase, we are able to include all of the scattered light within the expanding conic section of the column atmosphere since the W m^{-2} of sunlight absorbed is the total energy projected onto the surface area of the model grid. To diagnose heating rates after the scattering calculation, the incident (deposited) flux for option *geom*, as calculated in A.28 using geometric values, is further increased so that we collect the incident flux of the expanded layer into a
240 standard area defined by the surface grid.

$$D_K^{\text{geom}} = D_K (1 + Z_K^{\text{geom}}/R)^2 \quad (\text{A.34})$$

Table S1. Variable list	
M	number of model layers
K = 1:M	index of a layer
L = 1:M+1	index of a layer edge
R	surface radius of the Earth (6371 km)
R _L	radius to layer edge L
Z _L	height of layer edge L; can be geopotential or geometric
g ₀	gravitational acceleration at the surface, $\sim 9.81 \text{ m s}^{-2}$
g(Z)	gravitational acceleration at altitude Z, the surface, $g_0/(1 + Z/R)^2$
Z ^{geop}	geopotential height, integrated using $g(Z) = g_0$
Z ^{geom}	geometric height
CA	column atmosphere
A _{CA}	solar zenith angle defined as the angle between the CA radius vector and a radius vector pointing at the sun, without refraction it is the angle of the sun at each layer
A _L	zenith angle along a ray path crossing layer edge L at radius R _L
A _{M+1}	zenith angle at top of the atmosphere
P(L, K)	the distance through layer K of the solar ray ending at radius R _L .
AMF(L, K)	air mass factor for layer K along the ray path to layer edge L. AMF = ratio of path length to layer thickness (R _{K+1} – R _K), always ≥ 1 .
N _K	index of refraction in layer K
sARN _L	shorthand for $\sin(A_{CA}) R_L N_L$, which is the invariant along the refracted light path
A' _M	zenith angle at the bottom of radius layer edge R _{M+1} , from the ray path connecting R _M (angle A _M) to R _{M+1} ; it is not equal to A _{M+1} the angle at the top of R _{M+1} because of refraction
R _L N _L	the path invariant (sARN _L) for the refracted ray path that has its tangent radius (i.e., is orthogonal to the radius) at radius R _L
A ^{tan} _L	zenith angle ($>90^\circ$) where the refracted ray is tangent to radius R _L , $\equiv A^{\text{tanS}}(\text{L}, \text{L})$
A ^{tanS} (L, K)	zenith angle where the refracted ray crosses each successive radius on the sunlit side, for refracted path with tangent radius R _L

$A^{\tan D}(L, K)$	zenith angle at radius R_K on the dark side, for refracted path with tangent radius R_L , $A^{\tan D}(L, -) = 2 A^{\tan L} - A^{\tan S}(L, -)$ is symmetric about the tangent point
$P^{\tan S}(L, K)$	path length of a refracted ray path through layer K on the sunlit side with a tangent radius of R_L .
$P^{\tan D}(L, K)$	dark-side refracted path lengths through layer K passing through tangent radius R_L , it is symmetric $P^{\tan D}(L, -) = P^{\tan S}(L, -)$
$A^{\tan D}(L, K)$	zenith angle at radius R_K on the dark side, for refracted path with tangent radius R_L
$dTAU_K$	extinction optical depth of layer K ($dTAU_K^{abs} + dTAU_K^{sca}$), can be designated either geop or geom , used to calculate the extinction of the solar beam (F_L)
$TTAU^L$	total opacity along path from layer L to the sun, include AMF, can be calculated from either geopotential or geometric dTAU, used to calculate F_L
F_L	intensity of sunlight at layer edge L, defined as 1 at top of atmosphere
$dSTAU_K$	extinction optical depth of layer K used in the 1D multiple scattering code
D_K	direct solar flux deposited in layer K; based on $F_{M+1} = 1$; if <i>geom</i> option, then must increase by factor $(1 + Z_K^{geom}/R)^2$
D_0	direct solar flux deposited at the surface